Neutron diffraction and x-ray resonant exchange-scattering studies of the zero-field magnetic structures of $TbNi_2Ge_2$

Zahirul Islam,* C. Detlefs,† A. I. Goldman, S. L. Bud'ko, and P. C. Canfield
Ames Laboratory and Department of Physics and Astronomy, Iowa State University, Ames, Iowa 50011

J. P. Hill, Doon Gibbs, T. Vogt, and A. Zheludev
Physics Department, Brookhaven National Laboratory, Upton, New York 11973
(Received 20 February 1998; revised manuscript received 27 May 1998)

The zero-field magnetic structures of the rare-earth intermetallic compound $TbNi_2Ge_2$ have been determined using conventional magnetic neutron diffraction and high-resolution x-ray resonant exchange scattering techniques. There are two distinct magnetic phase transitions in this material: one is from the high-temperature paramagnetic state to a *long period* antiferromagnetic phase at the Néel temperature ($T_N = 16.8$ K), and the other is at a lower temperature ($T_t = 9.3$ K), where the system locks into a *commensurate* phase. The structure above T_t is described by a *longitudinal, amplitude modulated, sinusoidal wave* with propagation vector $\boldsymbol{\tau}_1 \approx (000.758 \pm 0.002)$ in reciprocal-lattice units (r.l.u.). As the temperature is lowered below T_t, $\boldsymbol{\tau}_1$ locks at $(0\ 0\ \frac{3}{4})$ and additional magnetic Bragg reflections corresponding to $\boldsymbol{\tau}_2 = (\frac{1}{2}\ \frac{1}{2}\ 0)$ and $\boldsymbol{\tau}_3 = (\frac{1}{2}\ \frac{1}{2}\ \frac{1}{2})$ develop. A weak modulation $\boldsymbol{\tau}_1' = (0\ 0\ \frac{1}{4})$, related to $\boldsymbol{\tau}_1$ also appears indicating a squaring-up of the low-temperature structure. In this equal moment structure all Tb moments have the saturation value of $\mu_s = 9.0 \pm 0.2\mu_B$. Both the phases are uniaxial with Tb moments parallel to the $\hat{\mathbf{c}}$ axis of the tetragonal unit cell. [S0163-1829(98)03638-8]

I. INTRODUCTION

The ternary rare-earth intermetallic compounds with composition RT_2X_2, where R stands for a rare-earth element, T represents a transition-metal ion, and X denotes Si or Ge, display a wide variety of magnetic phenomena.[1,2] With the general exception of the T=Mn compounds which exhibit ferromagnetism, most of these materials, with moment-bearing R ions, show antiferromagnetic ordering at low temperature with virtually all of the magnetism associated with the R ions. Since the R ions in these compounds are well separated from each other, direct exchange is negligible. Due to their metallic nature, however, the magnetic interaction between two such ions can take place via the polarization of the conduction band electrons as in the case of elemental rare-earth metals. While this indirect exchange interaction (Ruderman-Kittel-Kasuya-Yosida, RKKY) is responsible for the long-range magnetic ordering, anisotropy (uniaxial or planar) is typically determined by crystalline electric field (CEF) effects which play an important role in these compounds. In addition to paramagnetism and magnetic ordering, intermetallics with Ce, Sm, Eu, and Yb also display correlated electron effects, some of which are manifested as heavy fermion superconductivity.[1]

Among this vast class of compounds, the RNi_2Ge_2 family of materials is of particular interest. Their magnetic properties are similar to the RNi_2Si_2 series, which displays considerable magnetocrystalline anisotropy. Until recently, however, magnetization measurements of the RNi_2Ge_2 compounds have been carried out only on polycrystalline samples where the information about anisotropy was not obtainable due to powder averaging. The magnetic structures of some of the members of this family have been determined using neutron-diffraction techniques on powder samples where the results, in some cases, are contradictory. For instance, the magnetic structure of $HoNi_2Ge_2$ was reported[3] to be incommensurate below T_N (6 K) with a modulation vector of the form $(0\ 0\ \tau_z)$ and moments in the tetragonal basal plane (a flat spiral), while another group[4] found the modulation to be of the form $(\tau_x\ \tau_y\ \tau_z)$ below a transition temperature of 4.8 K with moments at an angle of 42° from the unique tetragonal axis.

The need for systematic studies of single crystals seems clear in order to obtain a correct understanding of anisotropy and magnetic structures in the RNi_2Ge_2 materials. Single crystals of all members of this family, except $PmNi_2Ge_2$, have been grown at Ames Laboratory. Measurements of macroscopic properties, such as electrical resistivity and magnetization, have been carried out on these single-crystal samples in order to characterize their anisotropic behavior as a function of a rare-earth element. These results will be published elsewhere.[5] As a part of this series-wide study, a detailed examination of the temperature- and field-dependent magnetic structures of a particularly interesting member, $TbNi_2Ge_2$, was initiated. In this paper we present the zero-field magnetic structures of this material. The correct determination of these structures will allow an examination of the complex interplay between long-range magnetic order and local moment anisotropies as well as provide a starting point for investigations of the field-induced structures discussed below.

II. PREVIOUS INVESTIGATIONS OF THE MAGNETIC STRUCTURES

$TbNi_2Ge_2$ crystallizes in the body-centered tetragonal $ThCr_2Si_2$ structure (Fig. 1) with space group $I4/mmm(D_{4h}^{17})$

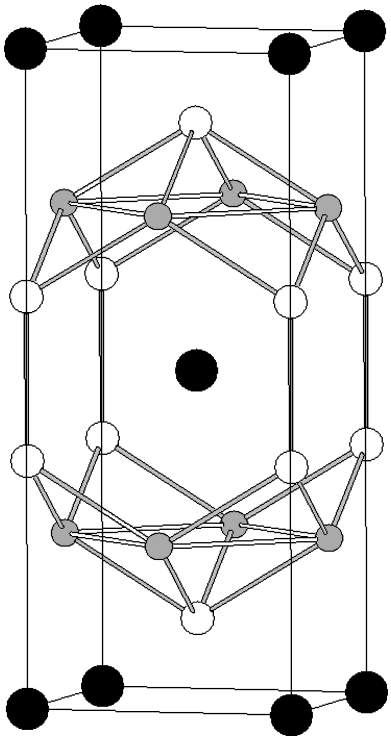

FIG. 1. A conventional unit cell of $TbNi_2Ge_2$ crystal. The large black circles denote Tb atoms, the small shaded circles represent Ni atoms, and the white circles stand for Ge atoms.

(see Ref. 6). Wyckoff positions of Tb atoms are $2(a)$ with point symmetry D_{4h} whereas Ni atoms are at $4(d)$. Two Ge atoms are positioned, one above and one below each Tb atom, at Wyckoff sites $4(e)$. In a conventional tetragonal unit cell the Tb atoms are located at the corners and body center, while the Ni atoms are positioned on the cell faces. This layered structure can be visualized as Tb planes separated along the $\hat{\mathbf{c}}$ axis by a network of Ni and Ge atoms. These atoms form a polyhedron surrounding each Tb atom located at the polyhedron center as depicted in Fig. 1.

Pinto *et al.* have studied a large number of RT_2X_2 rare-earth intermetallic ternaries, including $TbNi_2Ge_2$, using neutron diffraction from polycrystalline samples.[3] In $TbNi_2Ge_2$ they observed two transitions, at $T_N=16$ K and $T_t=9$ K, respectively. According to their work the structure below T_N is *incommensurate*. However, a complete determination of the structures was not carried out.

Later, in a more detailed study, Bourée-Vigneron[7] also found two transitions, at $T_N=17$ K and $T_t=10.25$ K, respectively. According to this study the magnetic structures in both the phases are *commensurate* with Tb moments aligned with the $\hat{\mathbf{c}}$ axis. The higher temperature structure is an *amplitude modulated* (AM) *logitudinal sine wave* with wave vector $(0\ 0\ \frac{3}{4})$ (Ref. 8) in reciprocal-lattice units (r.l.u.). Below T_t, additional satellite peaks corresponding to $(0\ 0\ \frac{1}{4})$ related to $(0\ 0\ \frac{3}{4})$ and a new wave vector $(\frac{1}{2}\ \frac{1}{2}\ \frac{1}{2})$ also develop. In this phase, the $(0\ 0\ \frac{3}{4})$ structure is a partially squared-up AM, similar to that above T_t. In addition, there are antiferromagnetically ordered Tb planes which account for the $(\frac{1}{2}\ \frac{1}{2}\ \frac{1}{2})$ modulation. A complete magnetic unit cell of the model structure for this phase is not given in Ref. 7. Refinement of this model, however, leads to values of the Tb^{3+} moment up to $12.45\pm0.35\mu_B$ at some sites, which is 40% larger than the saturated value of $9.0\mu_B$ expected for the ionic moment.

Although it is possible to have an excess moment associated with the spin polarization of the conduction-band electrons,[9] such a large enhancement of the moment is surprising. To illustrate the magnitude of the polarization contribution, we consider the isostructural $GdRh_2Si_2$ compound where the enhancement is solely due to exchange interactions since the Gd^{3+} ground state ($^8S_{7/2}$) is unaffected by CEF effects. In this case the polarization of the $5d$ conduction band contributes a maximum of $0.28\pm0.03\mu_B$ in excess of the Gd moment.[10]

III. CRYSTAL GROWTH AND MAGNETIZATION

The single crystals of $TbNi_2Ge_2$ used for our studies were grown at Ames Laboratory using a high-temperature flux growth technique.[11] These crystals have a platelike habit with the flat face perpendicular to the crystallographic $\hat{\mathbf{c}}$ axis. To detect the presence of any other phases, single crystals were pulverized and an x-ray powder-diffraction pattern was taken at room temperature, confirming the structure to be of $ThCr_2Si_2$ type with unit cell parameters a and c of 4.047 and 9.785 Å, respectively. No other phases were observed within the detectability limit ($\lesssim5\%$) of our measurements. This material was then characterized by anisotropic magnetization measurements using a Quantum Design MPMS-5 superconducting quantum interference device magnetometer which provides a temperature range of 1.8–350 K and a magnetic field up to 55 kG.

The temperature dependence of the low-field susceptibility $[\chi(T)]$ with applied field parallel ($\mathbf{H}\|\hat{c}$) and perpendicular ($\mathbf{H}\perp\hat{c}$) to the $\hat{\mathbf{c}}$ axis was found to be strongly anisotropic. From cusps in the susceptibility two transitions were identified which are indicated in Fig. 2(a). The paramagnetic to antiferromagnetic transition occurs at 16.7 K $T(_N)$. The second transition is at a lower temperature of 9.6 K (T_t). These transition temperatures are consistent with previously published results.[3,7]

Perhaps the most interesting behavior was found in the magnetization $[M(\mathbf{H})]$ as a function of field applied along the $\hat{\mathbf{c}}$ axis at 2 K [Fig. 2(b)]. As the field was increased from zero to its maximum value, a sequence of well-defined steps appeared. Up to 55 kG, five distinct transitions were observed (at 14, 18.1, 29, 35, and 45.8 kG, respectively). When the magnetization data was normalized to magnetic moment per Tb^{3+} ion, the sequence of magnetization values in the metamagnetic phases was approximately $\frac{1}{8}$, $\frac{1}{5}$, $\frac{3}{10}$, $\frac{1}{2}$, and $\frac{3}{5}$ of the saturation moment of $9.0\mu_B$. In Ref. 5 we find a transition to a seventh phase at 59 kG with $9.0\mu_B$ per Tb^{3+} which persists up to the maximum attainable field of 180 kG. Also, $M(\mathbf{H})$ is hysteretic and on field ramping down from the maximum value we find two more states, giving up to nine well-defined phases. When the applied field was in the basal plane, however, magnetization did not exhibit any transitions.

This anisotropic behavior is similar to that observed in the isostructural $TbNi_2Si_2$ compound[12,13] which is a likely can-

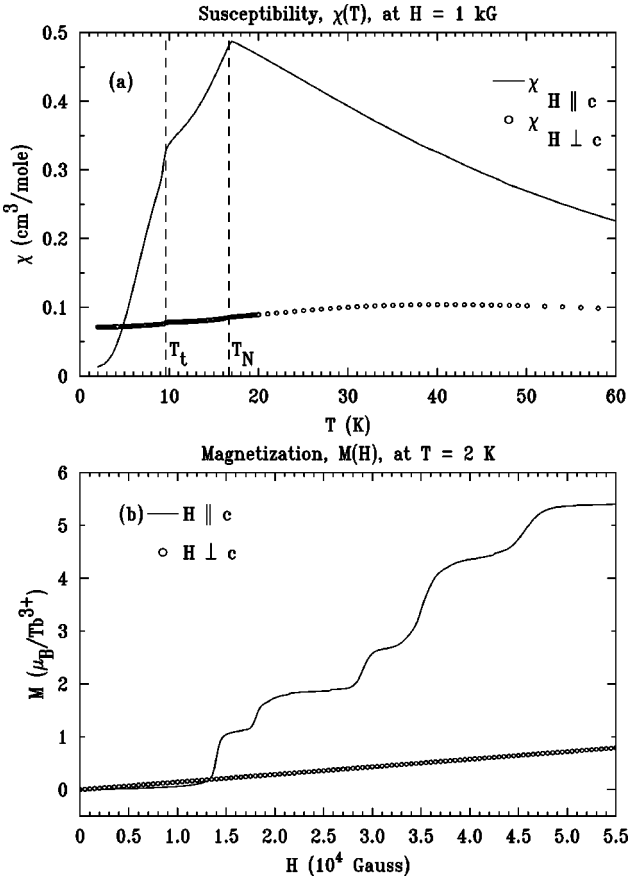

FIG. 2. (a) Susceptibility as a function of temperature at 1 kG and (b) magnetization as a function of field at 2 K of $TbNi_2Ge_2$ single crystal.

didate for a physical system exhibiting ''devil's staircase''[14] type behavior. In zero field, $TbNi_2Si_2$ is an *incommensurate* AM antiferromagnet below 15 K. At about 9 K, the structure locks into a *commensurate equal moment* (EM) phase (see Refs. 12,13, and references therein). In both the phases Tb moments are aligned with the $\hat{\mathbf{c}}$ axis. The most striking behavior was found[12] at 1.3 K, where five metamagnetic transitions were seen in an external field applied along the $\hat{\mathbf{c}}$ axis, although these transitions were not as clearly resolved as in Fig. 2(b), suggesting that $TbNi_2Ge_2$ is a better candidate for study. Neutron diffraction on a single crystal of $TbNi_2Si_2$ in a field revealed a rich phase diagram.[13] Among various phases, a field-induced transition into an AM structure from an EM phase was reported. Based on the similar magnetic properties and the isostructural relationship we expect a rich magnetic phase diagram for $TbNi_2Ge_2$ as well. Differences are likely to arise, however, due to the change in the environment of the Tb atoms brought about by Ge substitution for Si and by the different lattice parameters, since the oscillatory exchange interactions are very sensitive to magnetic ion-ion separation. Also, the number and clarity of states make $TbNi_2Ge_2$ an ideal system to study metamagnetic structures. But first it is vital to have a clear understanding of the zero-field structures. This is the focus of the rest of this paper.

IV. MAGNETIC NEUTRON DIFFRACTION FROM A SINGLE CRYSTAL

The neutron-scattering measurements on a single crystal of $TbNi_2Ge_2$ were carried out at the H4M spectrometer of High Flux Beam Reactor (HFBR) at Brookhaven National Laboratory. Neutrons with energies of 14.7 and 30.5 meV were used. Most of the work was carried out at 30.5 meV with collimator settings of $40'-40'-40'-40'$. A pyrolytic graphite filter was placed after the sample to eliminate second harmonic ($\lambda/2$) contamination of the beam. The largest crystal (166 mg) of the same batch as that used for the susceptibility measurements was chosen. No special preparation of the sample was necessary.

The single crystal was aligned with the $[h\ \ h\ \ l]$ zone in the scattering plane in order to identify all modulation vectors unambiguosly. At 20 K, above T_N as determined from the susceptibility data, scans along various symmetry directions in this zone showed only nuclear peaks consistent with body-centered crystal structure (i.e., $h+k+l=2n$ where n is an integer). Below T_N but above T_t, magnetic satellite peaks $(h\ \ h\ \ 0)\pm\boldsymbol{\tau}_1$ where $\boldsymbol{\tau}_1=(0\ \ 0\ \ \frac{3}{4})$ developed. The absence of any magnetic peaks of the form $(0\ \ 0\ \ l)\pm\boldsymbol{\tau}_1$ indicates that the ordered moment direction is along the $\hat{\mathbf{c}}$ axis.

At 4.7 K, below the second transition at T_t as determined from the susceptibility data, additional superlattice peaks associated with $\boldsymbol{\tau}_2=(\frac{1}{2}\ \ \frac{1}{2}\ \ 0)$ and $\boldsymbol{\tau}_3=(\frac{1}{2}\ \ \frac{1}{2}\ \ \frac{1}{2})$ were observed. A weak modulation, $\boldsymbol{\tau}_1'=(0\ \ 0\ \ \frac{1}{4})$, related to $\boldsymbol{\tau}_1$ also developed indicating a squaring-up of the structure. No other modulations in this zone were found. Again, the absence of $\boldsymbol{\tau}_1$ and $\boldsymbol{\tau}_1'$ magnetic satellites of $(0\ \ 0\ \ l)$ nuclear peaks implied that the ordered moments associated with these modulations are aligned with the $\hat{\mathbf{c}}$ axis. However, there remains the possibility of a component of the ordered moments in the basal plane associated with $\boldsymbol{\tau}_2$ and $\boldsymbol{\tau}_3$ modulations which we will discuss below.

The integrated intensities (order parameters) of various magnetic Bragg peaks corresponding to $(1\ \ 1\ \ 0)+\boldsymbol{\tau}_1$, $(0\ \ 0\ \ 0)+\boldsymbol{\tau}_2$ and $(0\ \ 0\ \ 0)+\boldsymbol{\tau}_3$ are shown in Fig. 3 as a function of temperature. For comparison the integrated intenstiy of the (1 1 2) nuclear peak is also shown which has no significant variation as the temperature is changed. The intensity of the $\boldsymbol{\tau}_1$ satellite increases from zero at T_N and shows a marked discontinuity in its slope at T_t. Simultaneously, magnetic peaks corresponding to $\boldsymbol{\tau}_2$ and $\boldsymbol{\tau}_3$ appear at T_t. These show very similar dependence on temperature, suggesting that they most likely originate from the same features of the structure. The transition temperatures obtained by modeling the magnetic order parameters by Brillouin-type functions $[B_{J=6}(|T-T_c|)$, where T_c is the transition temperature, see Fig. 3] are $T_N=16.8\pm0.2$ K and $T_t=9.8\pm0.3$ K, respectively, in close agreement with those determined by susceptibility measurements. We note the large enhancement of the integrated intensity of the $\boldsymbol{\tau}_1$ satellite below T_t.

Assuming a common origin for the symmetry inequivalent modulations $\boldsymbol{\tau}_2$ and $\boldsymbol{\tau}_3$, as suggested by the order-parameter measurements, we can compare the intensities of some satellites corresponding to these wave vectors to infer

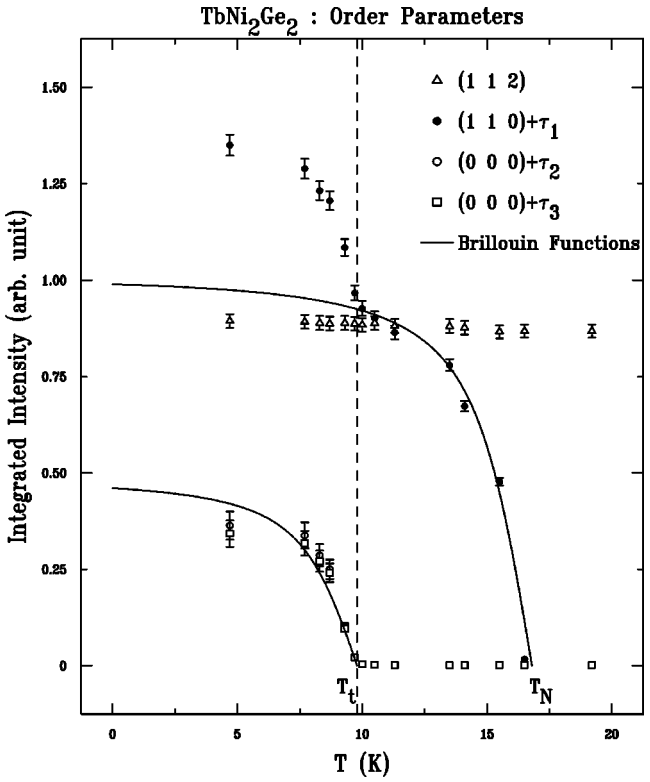

FIG. 3. Temperature dependence of various magnetic reflections measured by neutron diffraction ($E_{\text{neutron}}=14.7$ meV) on a single crystal. Data were collected on raising the temperature.

the ordered moment direction associated with them. We find that the intensities of these noncollinear Bragg peaks fell off as $I_{(3/2\ 3/2\ 0)}>I_{(3/2\ 3/2\ 1/2)}>I_{(3/2\ 3/2\ 3/2)}$ at a faster rate than the decrease that would be expected from the change in the magnetic form factor of Tb^{3+}. This behavior, combined with the large anisotropy in the susceptibility and the low-temperature magnetization measurements, suggests that the direction of ordered moments associated with these modulations in the low-temperature phase is also along the $\hat{\mathbf{c}}$ axis.

The temperature dependence of the weak $\boldsymbol{\tau}_1'$ satellite is shown in Fig. 4. We see that the intensity of this satellite

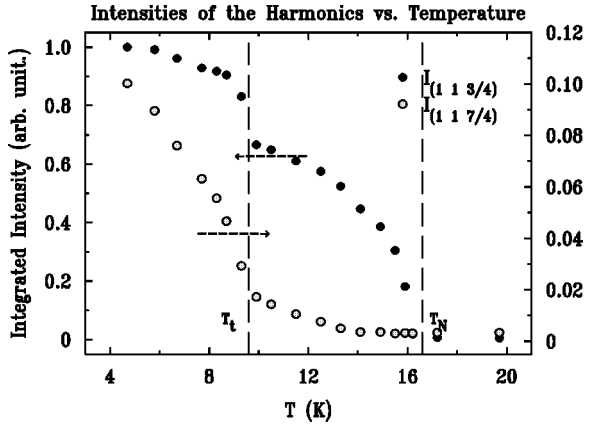

FIG. 4. Temperature dependence of $(1\ 1\ 0)+\boldsymbol{\tau}_1$ and $(1\ 1\ 2)-\boldsymbol{\tau}_1'$ as measured by neutron diffraction ($E_{\text{neutron}}=30.5$ meV) on a single crystal. Both the scales correspond to the same arbitrary unit. Data were collected on raising the temperature.

drops off at a much faster rate with temperature and becomes negligibly small above T_t. At the lowest temperature of 4.7 K, the ratio $I_{(0\ 0\ 1/4)}/I_{(0\ 0\ 3/4)}\approx 1/10$ which should be compared with $(\frac{1}{3})^2$ expected for the ratio of the third order and the fundamental components of a perfect square wave.

The data can be summarized as follows: below T_t, there are three magnetic modulation vectors, namely, $\boldsymbol{\tau}_1=(0\ \ 0\ \ \frac{3}{4})$, $\boldsymbol{\tau}_2=(\frac{1}{2}\ \ \frac{1}{2}\ \ 0)$ and $\boldsymbol{\tau}_3=(\frac{1}{2}\ \ \frac{1}{2}\ \ \frac{1}{2})$. The weak modulation $\boldsymbol{\tau}_1'=(0\ \ 0\ \ \frac{1}{4})$ is found to be the third harmonic of $\boldsymbol{\tau}_1$. For $T_t<T<T_N$, however, there is only one propagation vector, $\boldsymbol{\tau}_1$. Although $\boldsymbol{\tau}_2$ and $\boldsymbol{\tau}_3$ are not related by symmetry, similarities in temperature dependence of their integrated intensities suggests a common origin. Since $\boldsymbol{\tau}_2$ is a high-symmetry point of the Brillouin zone, we believe that the $\boldsymbol{\tau}_3$ modulation is likely to be a consequence of $\boldsymbol{\tau}_2$. On the other hand, the $\boldsymbol{\tau}_1$ modulation is independent and is the only ordering vector in the range $T_t<T<T_N$. In both the phases, the ordered moments are parallel to the $\hat{\mathbf{c}}$ axis.

V. X-RAY RESONANT EXCHANGE SCATTERING

In order to take advantage of the higher **Q** resolution available with x-ray scattering techniques, and to further test the x-ray resonant exchange scattering (XRES) cross section used to determine moment directions in magnetic compounds,[15,16] we have studied a single-crystal sample of $TbNi_2Ge_2$ by XRES. In recent experiments this technique has been successfully used to determine moment directions in the Gd, Nd, and Sm members of the RNi_2B_2C intermetallic compounds.[17,18]

These studies were performed on the X22C beamline at the National Synchrotron Light Source. This beamline utilizes a Ni-coated toroidal mirror to focus the x-ray beam at the sample position and reject higher harmonics in the incident beam. The incident energy was selected using a double bounce Ge(111) monochromator with an energy resolution of approximately 10 eV. The focused monochromatic beam at the sample position had a spot size of approximately 1 mm$\times$1 mm. In this configuration the flux was approximately 10^{11} photons/s at 8 KeV.

For the XRES experiment, a platelet of the $TbNi_2Ge_2$ crystal, from the same batch as that used for neutron-diffraction measurements, was mechanically polished perpendicular to the $\hat{\mathbf{c}}$ axis to eliminate surface contamination from the residual flux and to increase the reflectivity. The sample was cut perpendicular to the $\hat{\mathbf{a}}$ axis to have the final shape of a long narrow rectangular block with approximate dimensions of $5.0\times1.0\times0.5$ mm^3. This shape allowed Bragg peaks in the $[h\ \ 0\ \ l]$ zone to be conveniently studied. The narrow profile also ensured that the sample was completely bathed in the incident beam at all angles. The crystal was sealed inside a Be can filled with He gas and cooled in a closed cycle Heliplex-4 cryostat with a base temperature of 3.7 K. Integrated intensities were measured using a liquid-nitrogen cooled Ge solid-state detector. The sample mosaic at (0 0 6) was approximately 0.05°.

In order to use the resonant enhancement of the magnetic peaks, the primary beam energy was tuned to the L_{III} absorption edge of Tb where resonant enhancement is expected to

be the largest.[15,19,20] Above T_N, only charge peaks consistent with the body-centered-tetragonal structure were observed. Below T_t, careful scans along [0 0 1] direction revealed superlattice peaks corresponding to $\boldsymbol{\tau}_1$ and $\boldsymbol{\tau}_1'$ as was found in neutron-diffraction measurements. For $T_t<T<T_N$, however, the $\boldsymbol{\tau}_1'$ satellite disappeared and $\boldsymbol{\tau}_1$ was observed to shift toward (0 0 0.758) [see Fig. 8(a)]. We will discuss this behavior in detail shortly.

Energy scans of the $\boldsymbol{\tau}_1$ magnetic peaks were taken through the L_{III} absorption edge to observe the resonant enhancement and to confirm the magnetic nature of these satellites. These scans of the $(0\ 0\ 8)^+$ (superscript ''+'' denotes a $\boldsymbol{\tau}_1$ satellite) magnetic satellite and the (0 0 4) charge Bragg peak are shown in Figs. 5(a) and 5(b), respectively. The inflection point of the fluorescence yield [shown in Fig. 5(c)] was used to define the absorption edge ($E_{L_{\mathrm{III}}}$). A large resonant enhancement of the intensity (a factor of $\approx$55 relative to the intensity at 25 eV below the edge) was seen a few eV above the edge, which is the signature of electric dipole ($E1$) resonance involving electronic transitions, $2p_{3/2}\leftrightarrow 5d$. Similar resonant enhancement was also observed (a factor of $\approx$26 in this case) in the vicinity of the L_{II} edge. Due to the larger enhancement at the L_{III} edge, however, XRES measurements described below were taken at the resonant energy [dashed line at E_{res} in Fig. 5(a)] above this edge. Polarization analysis of magnetic scattering was not performed.

Longitudinal scans of $(0\ 0\ 10)^+$ magnetic satellite at selected temperatures are shown in Fig. 6. The most notable feature in these measurements is the shift of the peak position to higher Q value as the temperature increases, suggesting a change in the modulation vector. Since the lattice parameter c does not change appreciably with temperature (see Fig. 7) this shift reflects a change in $\boldsymbol{\tau}_1$.

The Bragg peak intensities (I_{Max}), widths (half width at half maximum, HWHM) and the modulation vectors obtained as a function of temperature are shown in Fig. 8. The main result of our XRES measurements is the temperature dependence of the $\boldsymbol{\tau}_1=(0\ \ 0\ \ \tau_z)$ propagation vector [Fig. 8(a)]. Below T_t, it remains locked at $(0\ \ 0\ \ \frac{3}{4})$ as was found in neutron measurement. However, above T_t it changes to (000.758 ± 0.002), within a temperature inteval of 0.25 K. The neutron-diffraction measurements were not able to resolve this steplike feature. In the temperature range $T_t<T<T_N$, the modulation vector $\boldsymbol{\tau}_1$ remains nearly constant within the error bars making it difficult to say whether the structure is *higher-order commensurate* or *incommensurate*.

As shown in Figs. 8(b) and 8(c) both I_{Max} and HWHM show a discontinuity at the second phase transition from which T_t is found to be 9.3 ± 0.2 K. It is surprising, however, that the magnetic peak broadens, corresponding to a reduced correlation length, at the transition to a commensurate phase. The measured longitudinal linewidth of the (0 0 6) charge peak is ±0.0038 r.l.u. and is indicated by the dotted-dashed line in Fig. 8(c) for comparison. The rocking curve width of the $(0\ 0\ 8)^-$ satellite (not shown) is equal to the sample mosaic at (0 0 6), both of which are independent of temperature. We can compare the magnetic correlation lengths of the ordered phases by assuming that they are given simply by the inverse of the peak width (HWHM) in $\mathrm{\AA}^{-1}$ corrected for the instrumental resolution. Since the instrumental q resolution was not measured we assume that it is the same as the charge peak linewidth. At 3.7 K, in the commensurate phase, the magnetic correlation length is then 600 Å whereas at 9.75 K, in the higher temperature phase, it is on the order of 1200 Å.

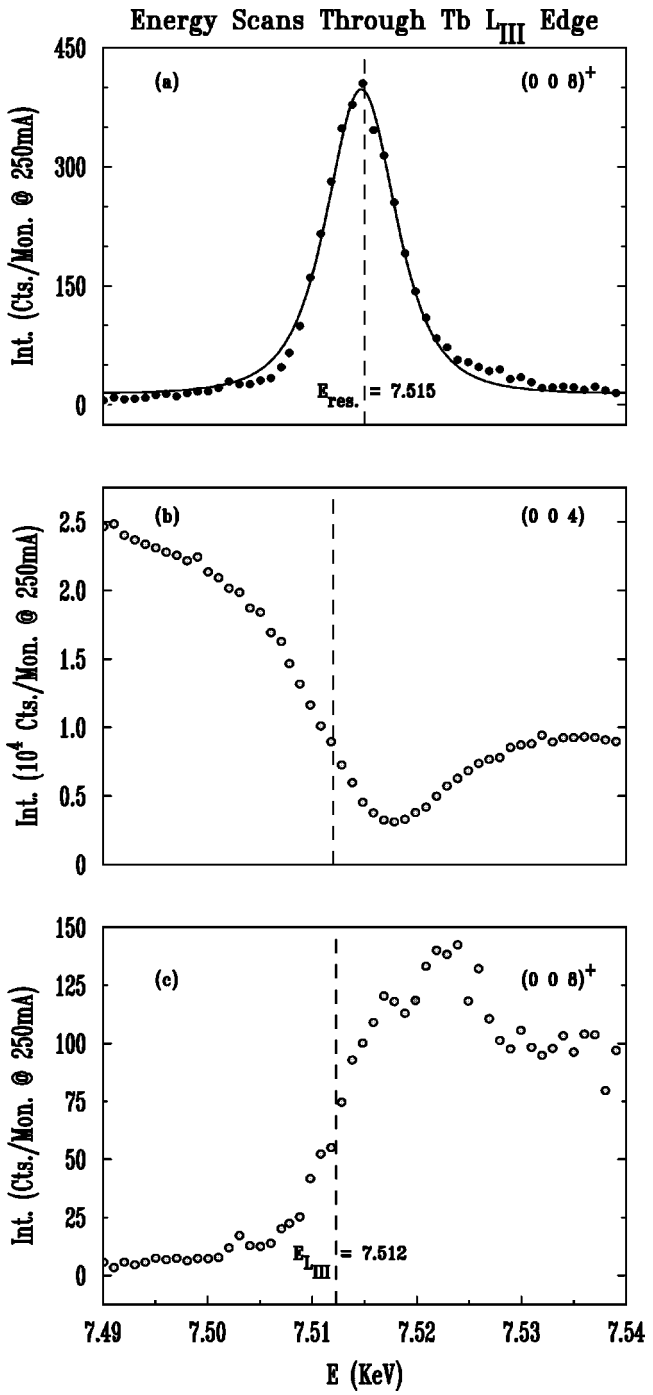

FIG. 5. Energy scans through the L_{III} edge of Tb at $T=3.7$ K. (a) $(0\ 0\ 8)^+$ magnetic satellite peak, (b) (0 0 4) charge Bragg peak, and (c) fluorescence yield used to define the absorption edge. Solid line in (a) is a Lorentzian squared fit used to obtain the resonant energy.

The integrated intensity (I) of the $(0\ 0\ 10)^+$ satellite peak is shown in Fig. 8(d) as a function of temperature, complementing similar measurements by neutron diffraction. The Néel temperature (T_N) determined by modeling the tem-

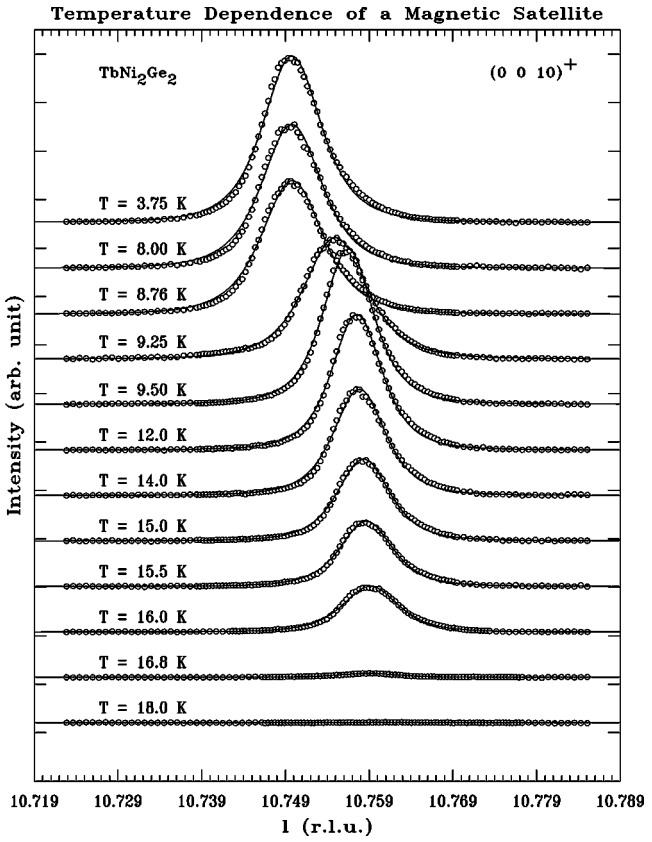

FIG. 6. Longitudinal scans of the $(0\ 0\ 10)^+$ magnetic satellite peak at selected temperatures. Note the shift of the peak position to higher Q as the temperature is raised above T_t. Solid lines are fits to Lorentzian squared line profiles used to extract I_{Max}'s, HWHM's, and peak positions. 1 r.l.u.$=0.6424$ Å^{-1}.

perature dependence with a Brillouin function $[B_{J=6}(|T-T_N|)]$ is 16.8 ± 0.2 K. As was true for the order parameters measured by neutrons, there is a break in slope at T_t and the intensity is significantly enhanced at low temperature.

The directions of the ordered Tb moments were also determined by XRES from the **Q** dependence of the integrated

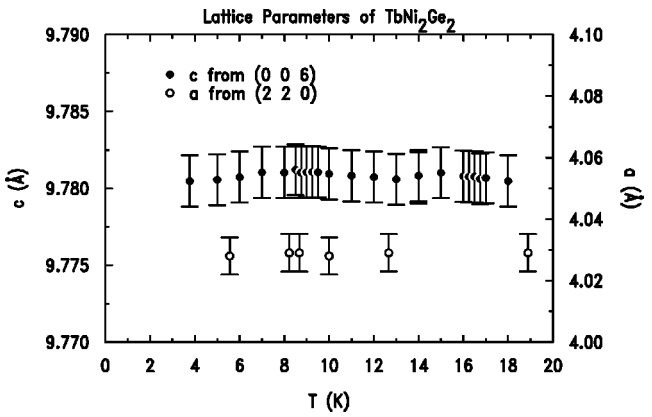

FIG. 7. Temperature dependence of the c lattice parameter as obtained from the (0 0 6) charge Bragg reflection in XRES measurements. Also shown is the lattice parameter a obtained from (2 2 0) reflection in neutron-diffraction measurements on a single crystal.

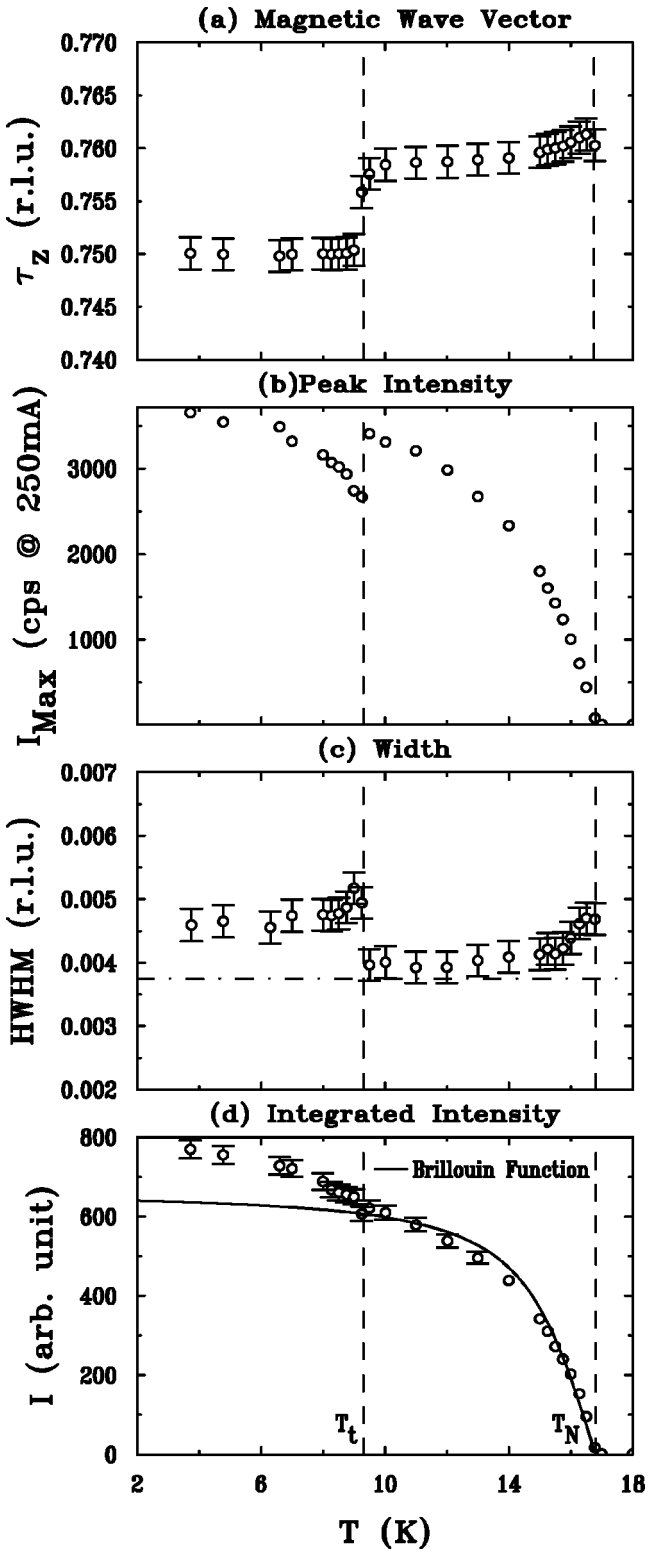

FIG. 8. Temperature dependence of (a) the modulation vector, $\tau_1=(0\ 0\ \tau_z)$; (b) Bragg peak intensity, I_{Max}; (c) width, HWHM, and (d) the order parameter, I. The horizontal dotted-dashed line in (c) shows the position of the assumed instrumental q resolution. Data were collected on raising the temperature.

intensities of a series of magnetic satellites. Figure 9 shows the **Q** dependence measured in the symmetric scattering geometry at 3.7 and 12 K for magnetic satellites of the form $(0\ 0\ l)^{\pm}$ ($\pm$ denotes a τ_1 satellite) along with model cal-

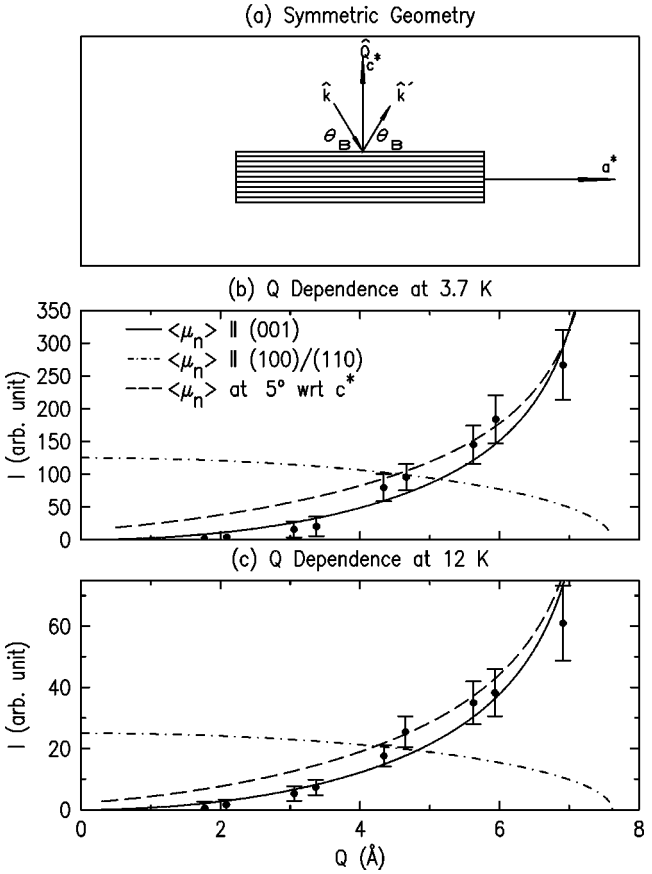

FIG. 9. **Q** dependence of the integrated intensities of magnetic Bragg peaks of the form $(0\ 0\ l)^{\pm}$ at (b) 3.7 K and (c) 12 K, respectively. Measured intensities are shown in filled circles. Solid line is for a model with Tb moments $\|\hat{\mathbf{c}}$ axis ($\beta=0$), dotted-dashed line is for moments $\perp\hat{\mathbf{c}}$ axis ($\beta=90°$), and the dashed line is for $\beta=5°$. Scattering geometry is shown in panel (a).

culations. For the electric dipole ($E1$) resonance the integrated intensity of a magnetic Bragg peak ($h\ k\ l$) is given by (ignoring the Debye-Waller factor):[16–18]

$$I_{hkl}^{\mathrm{XRES}} \propto \frac{\sin(\theta_{\mathrm{B}})}{2\mu\sin(2\theta_{\mathrm{B}})}|\hat{k}'\cdot\hat{z}_n|^2. \tag{5.1}$$

The Lorentz velocity factor, $1/\sin(2\theta_{\mathrm{B}})$, and the angular factors to account for the absorption and for the fraction of the beam intercepted by the sample are also included. $\hat{k}'$ is the direction of the scattered beam, μ is the linear absorption coefficient at a given energy, and $\hat{z}_n$ is the direction of the magnetic moment ($\langle\mu_n\rangle$) at the nth site. The only adjustable parameter in the calculations is an arbitrary scale factor. As shown in Figs. 9(b) and 9(c), a model with the Tb moments in the basal plane results in a **Q** dependence manifestly in disagreement with the data, while for moments along the $\hat{\mathbf{c}}$ axis the **Q** dependence at both the temperature can be modeled quite well. We point out, however, that the XRES data is insensitive to variations of the tilt angle (β) of the moments away from the $\hat{\mathbf{c}}$ axis by about $\sim 5°$ [see the dashed line in Figs. 9(b) and 9(c)].

In summary, the principal finding of XRES experiment is the temperature dependence of $\boldsymbol{\tau}_1$, which moves to $\approx(0\ 0\ 0.758)$ at T_t, and remains nearly constant above this transition. Below T_t, $\boldsymbol{\tau}_1$ is locked at $(0\ 0\ \frac{3}{4})$. Also, we have seen a surprising broadening of the magnetic peak, corresponding to a reduced magnetic coherence length, at the phase transition from the higher temperature phase to the commensurate structure. In addition, we have used this technique to confirm the uniaxial ordering with the Tb moments parallel to the $\hat{\mathbf{c}}$ axis in both the ordered phases in agreement with the neutron-diffraction measurements.

VI. NEUTRON DIFFRACTION FROM POWDER

With the propagation vectors and the moment direction known from neutron, XRES and magnetization measurements on single-crystal samples, we used powder neutron-diffraction data to accurately determine the value of the ordered moments in order to eliminate uncertainities from single-crystal samples related to crystal shape and extinction effects. The procedure used and the assumptions made for the powder pattern calculations are briefly explained in the Appendix.

Polycrystalline samples for neutron-diffraction measurements were synthesized by arc-melting the stoichiometric mixture of the respective elements in an argon atmosphere and were subsequently annealed. The phase purity of the sample was verified by an x-ray powder-diffraction pattern. Susceptibility measured on this powder showed the Néel transition at the expected temperature ensuring that the magnetic ordering was not destroyed by strain during the grinding process although the transition at T_t was not clearly discernible. Neutron-diffraction measurements on this sample were performed at the high-resolution neutron powder diffractometer located at the HFBR. Neutrons with wavelength of 1.8857 Å were used. The sample was sealed in a cylindrical vanadium container of diameter 0.9 cm and cooled inside a pumped He cryostat. Diffraction patterns were collected at several temperatures over the angular range 0°–155° in 2θ with a step size of 0.05°. The zero of 2θ is defined within $\pm 0.05°$.

The neutron-diffraction patterns at three different temperatures for a selected range of angles are shown in Fig. 10. At 20 K, well above the transition temperature, only nuclear Bragg peaks corresponding to body-centered-tetragonal crystal structure were observed. Figure 10(a) shows a few such low angle nuclear peaks. A conventional unit cell was used to index these peaks with $a=4.04$ and $c=9.784$ Å, consistent with the lattice parameters determined from the single-crystal samples. In addition to sharp peaks, magnetic diffuse scattering is also seen at low angle region.

The calculated powder pattern at 20 K for the nuclear peaks, based upon published[6] structure for $TbNi_2Ge_2$ and the above lattice parameters, was found to be in very good agreement with the observed intensities, confirming the low-temperature crystal structure to be of $ThCr_2Si_2$ type. The overall index R-Bragg[21] was 7%. The scale factor (see the Appendix) thus found is used in the model calculations for the magnetic peaks in order to put them on an absolute scale with the nuclear peaks.

Above T_t, but below T_N, all of the magnetic peaks in the pattern [Fig. 10(b)] can be indexed using only $\boldsymbol{\tau}_1$

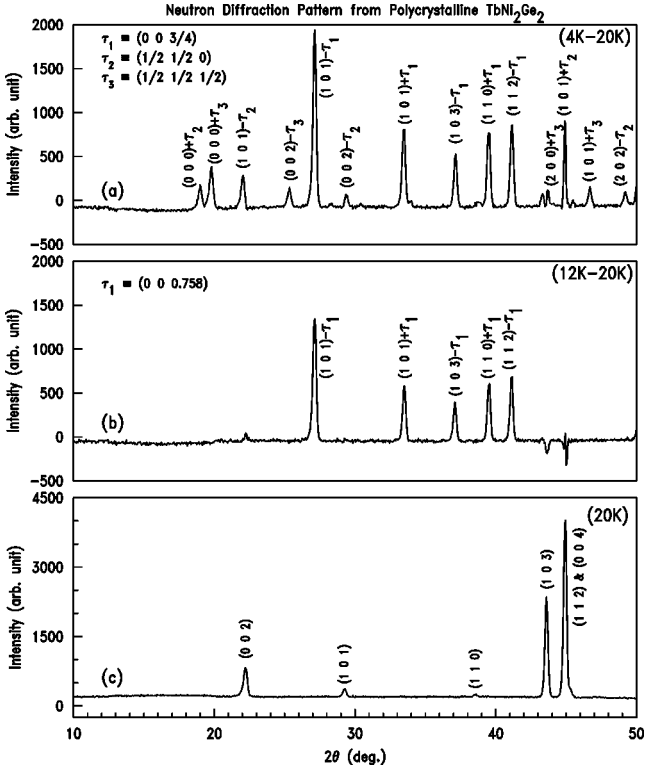

FIG. 10. Neutron-diffraction patterns from polycrystalline $TbNi_2Ge_2$ sample at (a) 4 K, (b) 12 K, and (c) 20 K. Diffraction pattern at 20 K was subtracted from those at 4 K and 12 K in order to identify the magnetic peaks. These are shown in (a) and (b). Indices of some of the weak peaks in (a) are not shown.

$=(0\ \ 0\ \ \ 0.758)$ modulation (see Table I). The small peak at the position of (0 0 2) is an artifact of the subtraction method, as are the ''negative'' peaks. As expected, the $\boldsymbol{\tau}_1$ satellites of $(0\ \ 0\ \ l)$ nuclear peaks are absent due to the fact that the moment direction is parallel to the $\hat{\mathbf{c}}$ axis in both magnetic phases. All of the superlattice peaks in the powder neutron-diffraction pattern at 4 K can be indexed [Fig. 10(c) and column $(h\ \ k\ \ l)_c \pm \boldsymbol{\tau}_{\rm mag}$ of Table II] using the wave vectors found in the measurements on single-crystal samples. This indicates that there are no additional modulations in this phase.

TABLE I. Observed and calculated intensities of selected magnetic Bragg reflections of $TbNi_2Ge_2$ at $T=12$ K. Superscript $+/-$ in the second column stands for a $\boldsymbol{\tau}_1$ satellite. Calculations of R-Bragg included more reflections not listed in the table.

No.	(hkl)	$Q(\text{Å}^{-1})$	$I_{\rm Obs}$	$I_{\rm Cal}$	$I_{(00\frac{3}{4})}$
1	$(1\ \ 0\ \ 1)^-$	1.5630	454±14	415±17	414±17
2	$(1\ \ 0\ \ 1)^+$	1.9218	183±6	171±7	172±7
3	$(1\ \ 0\ \ 3)^-$	2.1194	124±4	112±5	110±5
4	$(1\ \ 1\ \ 0)^+$	2.2527	181±6	168±6	169±6
5	$(1\ \ 1\ \ 2)^-$	2.3396	200±6	143±6	142±6
6	$(1\ \ 1\ \ 2)^+$	2.8239	64±2	60±3	60±3
7	$(1\ \ 0\ \ 3)^+$	2.8711	32±2	28±3	28±3
8	$(1\ \ 1\ \ 4)^-$	3.0286	41±2	43±3	43±3
9	$(2\ \ 0\ \ 2)^-$	3.2111	77±3	65±3	64±3
10	$(1\ \ 2\ \ 1)^-$	3.4811	120±4	108±5	108±5

Magnetic R-Bragg = 9.3%
Overall R-Bragg = 7.3%

Below T_t, a magnetic unit cell of the commensurate structure can be constructed by doubling the chemical unit cell along the (1 1 0) direction, implied by $\boldsymbol{\tau}_2$, and stacking four such groups of unit cells along (0 0 1) direction, implied by $\boldsymbol{\tau}_1$. All magnetic peaks can also be indexed with respect to this supercell.[22] These indices are shown in the second column of Table II [column $(h\ \ k\ \ l)_{\rm m}$].

The temperature dependence of $(\frac{1}{2}\ \ \frac{1}{2}\ \ 0)$, $(\frac{1}{2}\ \ \frac{1}{2}\ \ \frac{1}{2})$, $(0\ \ 0\ \ 10)^+$ and peaks of the form $(1\ \ 1\ \ l)^{\pm}$ was measured on the single-crystal sample. In Fig. 11 we plot the integrated intensity of the $(1\ \ 0\ \ 1)^-$ satellite peak as measured on the powder sample to obtain a unified picture. As was the case previously, the temperature dependence below T_N can also be modeled by a Brillouin function which yields a Néel temperature of 16.8 ± 0.3 K. Although there is a large enhancement of the intensity below T_t, the break in slope at this transition is less discernible than in the former cases.

The order parameter associated with $\boldsymbol{\tau}_1$, as observed at $(0\ \ 0\ \ 10)^+$ (Fig. 8), $(1\ \ 1\ \ 0)^+$ (Fig. 3), and $(1\ \ 0\ \ 1)^-$ (Fig. 11), respectively, has a marked discontinuity of the slope at T_t and a large increase of the low-temperature intensity relative to that above this transition. These can be explained as consequences of the Tb moments acquiring the full saturation value of $9.0\mu_{\rm B}$ below T_t from an AM phase above this temperature. If the structure remained AM below T_t a smoothly varying order parameter would be expected.

A. Amplitude modulated phase ($T_t<T<T_N$)

In this phase all the ordered moments in a given Tb plane (j) have the same magnitude and direction while they vary sinusoidally from plane to plane according to

$$\langle \boldsymbol{\mu}_j \rangle = \mu_s \cos(2\pi \boldsymbol{\tau}_1 \cdot \mathbf{r}_j + \phi)\hat{\mathbf{c}}, \tag{6.1}$$

where μ_s is the saturation moment ($9.0\mu_{\rm B}$) of Tb^{3+}, $\mathbf{r}_j$ is in units of lattice parameter c, and ϕ is an arbitrary phase factor. For intensity calculations $\boldsymbol{\tau}_1$ was approximated by $(0\ \ 0\ \ \frac{25}{33})$ and $\phi=0$ was used. We have assumed zero magnetic moments for the Ni atoms. The calculated intensities ($I_{\rm Cal}$) for this model agree quite well with the observed ones ($I_{\rm Obs}$) as shown in Table I. For comparison, we have listed some of the calculated intensities for an AM model with $\boldsymbol{\tau}_1 =(0\ \ 0\ \ \frac{3}{4})$ (column headed $I_{(0\ 0\ 3/4)}$) which is the model proposed in a previous experiment.[7] Although the agreement between this model and the powder pattern is as good as in our model's case the modulation vector is not correct as known from the XRES measurements.

B. Equal moment commensurate phase ($T<T_t$)

The model for the low-temperature ordered phase is shown in Fig. 12. As in the AM phase, we have assumed zero magnetic moments for the Ni atoms. As can be seen, while the ferromagnetic planes (such as 0–2 and 4–6) account for $\boldsymbol{\tau}_1$ and $\boldsymbol{\tau}_1'$, the antiferromagnetic planes (3 and 7) give rise to $\boldsymbol{\tau}_2$ and $\boldsymbol{\tau}_3$ superlattice peaks. It is evident from

TABLE II. Observed and calculated intensities of selected magnetic Bragg reflections of $TbNi_2Ge_2$ at $T=4$ K. Indices in the second and the third columns refer to the magnetic and chemical unit cell, respectively. The intensities in the case of overlapping peaks are given in the row for the strongest peak in the group. Calculations of *R*-Bragg included more reflections not listed in the table.

No.	$(h\ k\ l)_m$	$(h\ k\ l)_c \pm \tau_{mag}$	Q (Å^{-1})	I_{Obs}	I_{Cal}
1	(1 1 0)	(0 0 0)+τ_2			
	(1 1 2)	(0 0 0)+τ_3	1.1456	293±9	303±12
2	(1 1 6)	(0 0 2)−τ_3	1.4620	68±3	69±4
3	(2 0 1)	(1 0 1)−τ_1	1.5635	619±18	602±24
4	(2 0 7)	(1 0 1)+τ_1	1.9188	298±12	270±12
5	(2 0 9)	(1 0 3)−τ_1	2.1229	172±7	159±6
6	(2 2 3)	(1 1 0)+τ_1	2.2516	239±8	245±10
7	(2 2 5)	(1 1 2)−τ_1	2.3414	277±9	210±9
	(2 0 11)	(1 0 3)−τ_1'			
8	(2 2 9)	(1 1 2)+τ_1'			
	(3 1 3)	(1 0 1)+τ_3	2.6410	65±3	55±3
9	(1 1 16)	(0 0 4)+τ_2			
	(5 1 8)	(2 0 2)+τ_2			
	(2 2 11)	(1 1 2)+τ_1	2.8207	177±5	172±7
	(2 0 15)	(1 0 3)+τ_1			
10	(2 2 13)	(1 1 4)−τ_1	3.0321	57±2	62±3
11	(4 0 5)	(2 0 2)−τ_1	3.2124	87±3	95±4
12	(2 4 1)	(1 2 1)−τ_1	3.4813	150±5	164±7
13	(2 4 7)	(1 2 1)+τ_1	3.6547	121±4	134±5
	(3 3 10)	(1 1 2)+τ_3			
14	(5 1 8)	(2 0 2)+τ_2	4.1679	21±2	19±2
	(3 3 16)	(1 1 4)+τ_2			
15	(2 4 15)	(1 2 3)+τ_1	4.2301	75±3	59±3
16	(4 4 5)	(2 2 2)−τ_1	4.4715	31±2	36±2
17	(6 0 1)	(3 0 1)−τ_1	4.6685	31±2	32±2
Magnetic	*R*-Bragg = 8.7%				
Overall	*R*-Bragg = 6.8%				

Table II that the calculated intensities (I_{Cal}) according to this model agree very well with the observations. The value for the Tb ordered moment was found to be $9.0\pm0.2\mu_B$ which is the expected saturation value of the Hund's rule ground state ($^7F_6$) of Tb^{3+}.

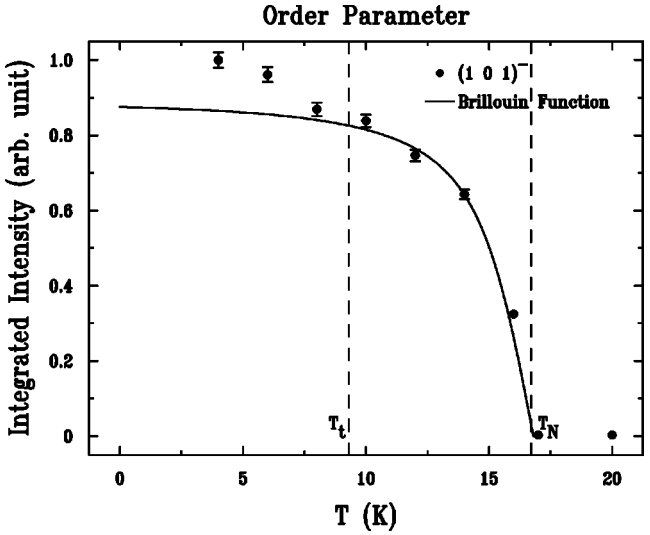

FIG. 11. Temperature dependence of the integrated intensity of $(101)^-$ magnetic peak measured by powder neutron diffraction.

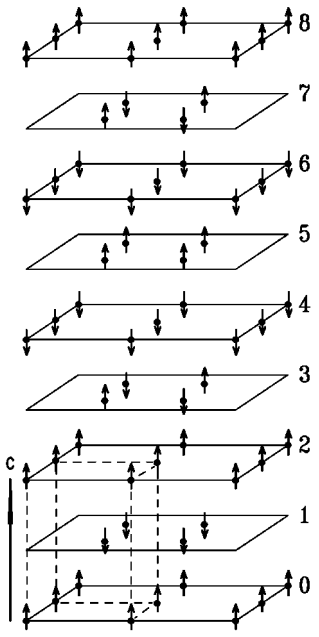

FIG. 12. The magnetic structure of $TbNi_2Ge_2$ at 4 K. One magnetic unit cell is shown. The dashed lines indicate a conventional unit cell. ↑(↓) represents magnetic moment of Tb (depicted by solid circles) ''up'' (''down'') along the $\hat{\mathbf{c}}$ axis. Ni and Ge atoms are not shown. Planes are numbered for reference.

We have also considered the possibility of induced moments ($\leqslant \frac{1}{2}\mu_B$) at the Ni sites which are ferromagnetically coupled to the Tb moments assuming only the nearest Tb-Ni pair interaction to be dominant. In this scheme induced moments can exist only on the Ni sites between planes such as 2 and 3 in Fig. 12. At all other Ni planes the exchange field vanishes by symmetry. The calculated intensities, however, were insensitive to the value of induced moment up to $0.3\mu_B$ and produced equally good fits. Above this value they disagreed with the observed ones. Thus, we place an upper bound of $0.3\mu_B$ for an induced moment at the allowed Ni sites.

VII. DISCUSSION

We have determined the zero-field magnetic structures of $TbNi_2Ge_2$ using neutron diffraction and XRES measurements. In the low-temperature ($T<T_t$) phase, propagation vectors $\boldsymbol{\tau}_1=(0\ 0\ \frac{3}{4})$ [along with the third harmonic $\boldsymbol{\tau}_1'=(0\ 0\ \frac{1}{4})$], $\boldsymbol{\tau}_2=(\frac{1}{2}\ \frac{1}{2}\ 0)$ and $\boldsymbol{\tau}_3=(\frac{1}{2}\ \frac{1}{2}\ \frac{1}{2})$ were identified by neutron diffraction on a single crystal. The subtle change of the wave vector $\boldsymbol{\tau}_1$ to (0 0 0.758) at T_t which was not detected in the earlier work[7] was resolved using the high-**Q** resolution of XRES. Above T_t it was difficult to determine whether the structure was *higher-order commensurate* or *incommensurate*. According to our model, the phase transition at T_t is from an EM *commensurate* phase ($T<T_t$) (Fig. 12) to an AM *long period* antiferromagnetic structure ($T_t<T<T_N$). From powder neutron-diffraction measurements, the magnitude of the Tb ordered moment in the EM phase was found to be $9.0\pm0.2\mu_B$. In the earlier work[7] the low-temperature phase was found to be AM. In both the phases the ordered moments of Tb were found to be parallel to the $\hat{\mathbf{c}}$ axis. In addition, we have placed an upper bound of $0.3\mu_B$ for any induced moments at Ni sites.[23]

An ordering vector of the form (0 0 τ_z) below T_N is common to several members of RNi_2Ge_2 family such as the Nd, Eu, Gd, Dy, Er, and Tm compounds. The modulation vectors reported for these materials below their respective ordering temperature (T_N) are (0 0 0.805),[24] (0 0 1),[25] (0 0$\approx$0.79),[25] (0 0$\approx$0.75),[26] (0 0 0.757),[4] and (0 0 0.7854),[27] respectively. The propagation vector $\boldsymbol{\tau}_1$ found in $TbNi_2Ge_2$ below T_N is consistent with this. We speculate that a ''nesting'' feature of the respective Fermi surfaces in these metallic systems at these wave vectors is responsible for the onset of magnetic ordering. Electronic band theoretical calculations to detect this feature are planned.

The low-temperature EM phase is an antiphase domain structure consisting of triplets of antiferromagnetically coupled ferromagnetic Tb planes (0–2 and 4–6 in Fig. 12) separated by planes ordered antiferromagnetically (3 and 7). The formation of triplets can be explained by a ferromagnetic coupling within the plane and two dominant interplanar coupling constants, nearest-neighbor antiferromagnetic, and next-nearest-neighbor ferromagnetic interactions. Since the modulation vector is (0 0 $\frac{3}{4}$) two such neighboring triplets have opposite phases. Due to the antiferromagnetic coupling between the nearest-neighbor planes the moments on planes such as 3 and 7 are ''frustated'' which can lead to antiferromagnetic ordering in these planes. In the pure AM phase above T_t this frustation is absent. Due to the presence of this ''frustation'' in the EM phase it is conceivable that the magnetic structure could break up into smaller domains compared to the domain sizes in the AM phase. This reduces the magnetic coherence length below T_t and can give rise to the magnetic peak broadening as was observed [Fig. 8(c)] in XRES measurements.

Although the mechanism driving the lock-in transition at T_t is not clear, it is interesting to consider a simple phenomenological model introduced by Elliot[28,29] which seems to account for the observed magnetic behavior of $TbNi_2Ge_2$. In his mean-field theory of an Ising model with a ferromagnetic in-plane coupling and interactions only between nearest- and next-nearest-neighbor planes, he shows that an AM structure is stable at finite temperature below the highest ordering temperature (T_N). This is because the free energy ($F=U-TS$) is lower due to higher entropy of the sinusoidal arrangement relative to that of an EM phase. As the temperature is lowered the entropic term decreases[30] and the stable structure is that which minimizes the internal energy, U. As a consequence, in this model, the modulated structure squares up and possibly changes into an antiphase domain structure at a temperature slightly above $\frac{1}{2}T_N$ where the moment saturates.[28,31] This general behavior is observed in both $TbNi_2Ge_2$ and $TbNi_2Si_2$ where the AM to an EM phase transition takes place at $T_t\sim0.55T_N$ and $T_t\sim0.6T_N$, respectively. According to this theory the magnetic specific heat (C_{mag}) at T_t would not show any sharp anomaly. Indeed C_{mag} measured[32] on $TbNi_2Si_2$ showed only a change in its slope at T_t consistent with a first-order transition involving a small latent heat. At T_N there was a large λ-type anomaly indicating the transition to be of second order. Specific-heat measurements of $TbNi_2Ge_2$ are clearly needed to investigate similar behaviors.

The ANNNI (axial/anisotropic nearest and next-nearest-neighbor Ising) model discussed above was extended by various authors.[14,33,34] According to their work a physical system such as $TbNi_2Ge_2$ should lock into an infinity of commensurate structures as some external parameter, such as the magnetic field, is varied giving rise to the so-called ''devil's staircase'' behavior. As discussed at the beginning of this paper there is a sequence of metamagnetic transitions in this material when a magnetic field is applied along the $\hat{\mathbf{c}}$ axis. We then expect to find a series of intricate field-induced phases. We speculate that the antiferromagnetic ''domain walls'' will be rearranged to give way to new periodicities as ferromagnetism is induced. Also of interest is a possible emergence of an AM structure from the low-temperature EM phase, as was reported to occur in $TbNi_2Si_2$ crystal.[13] These studies are presently in progress.

Finally, we point out that since Tb^{3+} is a non-Kramers ion it can have a singlet ground state due to the CEF splitting of its degenerate $J=6$ multiplet.[35] On the other hand, in order to form a large moment at low temperatures the presence of at least one low-lying CEF level at an energy comparable to the exchange energy above the ground state is also necessary.[36,37] These two levels can mix to form a ''compound'' ground state by the exchange interaction which varies in space according to the propagation vector. Since in the

case of $TbNi_2Ge_2$ the moments saturate in the EM phase the low-lying CEF eigenstates must also have a large $|J_z=\pm 6\rangle$ component where the axis of quantization, $\hat{\mathbf{z}}$, is along the direction ($\hat{\mathbf{c}}$ axis) of the ordered moments. Although CEF levels for $TbNi_2Ge_2$ are not known, for the isostructural $TbNi_2Si_2$ the ground state is a Γ_4^+ singlet with a Γ_3^+ singlet as the first excited state.[32] This excited state is only 6.6 K above the ground state and together they form a ''pseudodoublet.'' The measured entropy above T_N is $R\ln(2.4)$ which is consistent with this.[32] Other CEF levels are 38 K above the ground state. As was shown in Ref. 32, $|J_z=\pm 6\rangle$ predominates in both the low-lying singlets. The overall CEF splitting relative to the free-ion degenerate J multiplet is $\Delta\approx\pm 50$ K which is comparable to ≈ 40 K estimated from the susceptibility data[5] for $TbNi_2Ge_2$. Based on these similarities, a CEF level scheme such as that in $TbNi_2Si_2$ seems probable for $TbNi_2Ge_2$ which is likely to play an important role in various metamagnetic phases at low temperature.

ACKNOWLEDGMENTS

We thankfully acknowledge K. Myers for growing polycrystalline samples of $TbNi_2Ge_2$ for powder neutron-diffraction measurements. We would also like to thank B. N. Harmon for critical reading of the manuscript and C. Stassis for his comments. Ames Laboratory (U.S. Department of Energy) is operated by Iowa State University under Contract No. W-7405-Eng-82. This work was supported by the Director for Energy Research, Office of Basic Sciences. The work at Brookhaven Narional Laboratory was carried out under Contract No. DEAC0298CH10886, Division of Materials Science, U.S. Department of Energy.

APPENDIX: POWDER PATTERN CALCULATIONS

The intensity of a nuclear powder peak (hkl) was calculated according to[38,39]

$$I_{hkl}^N = S\frac{p_{hkl}^N}{\sin(\theta_B)\sin(2\theta_B)}\left|\sum_n \bar{b}_n e^{i\mathbf{Q}\cdot\mathbf{r}_n}\right|^2, \qquad \text{(A1)}$$

where S is an overall scale factor depending only on experimental conditions. All the other symbols have their usual meanings (see Refs. 38,39). We assumed corrections due to scattering extinctions, preferred orientations and strain broadening to be negligible. A small absorption correction[40] mostly due to Tb was found insignificant and was ignored. Also, since no significant thermal diffuse scattering was observed at these temperatures the Debye-Waller factor was ignored too.

For our calculations of magnetic peak intensities we used the following expression based on the same assumptions as for the nuclear case:[38,39,41]

$$I_{hkl}^M = \frac{S}{N_m^2}\frac{p_{hkl}^M}{\sin(\theta_B)\sin(2\theta_B)}\langle q^2\rangle\left(\frac{\gamma e^2}{2m_e c^2}\right)^2 \times\left|\sum_j \langle\boldsymbol{\mu}_j\rangle f_j(Q)e^{i\mathbf{Q}\cdot\mathbf{r}_j}\right|^2. \qquad \text{(A2)}$$

Here N_m is the number of chemical unit cells comprising the magnetic unit cell, $\langle\boldsymbol{\mu}_j\rangle$ is the thermal average of the magnetic moment (in Bohr magneton, μ_B) and all the other symbols have their usual meanings (see Refs. 38,39,41). The summation is over all the magnetic atoms of a magnetic unit cell. The magnetic form factors $[f_j(Q)]$ were calculated in the dipole approximation using analytic expressions given in Ref. 42.

There is only one temperature-independent overall scale factor (S) to ''fit'' which was determined from the nuclear data at 20 K and used to put magnetic peaks on an absolute scale in order to get the value of the ordered moments. None of the crystal structural parameters were refined. Observed intensities were obtained by simple numerical integrations corrected for constant background. When there were significant peak overlaps, intensities of all Bragg peaks were added.

*Electronic address: zahirul@iastate.edu
†Present address: ESRF, Grenoble, France.

[1] A. Szytula and J. Leciejewicz, *Handbook of Crystal Structures and Magnetic Properties of Rare Earth Intermetallics* (CRC Press, Boca Raton, 1994), pp. 114–192.
[2] A. Szytula and J. Leciejewicz, in *Handbook on the Physics and Chemistry of Rare Earths*, edited by K. A. Gschneidner, Jr. and L. Eyring (Elsevier Science, Amsterdam, 1989), Vol. 12, pp. 133–211.
[3] H. Pinto, M. Melamud, M. Kuznietz, and H. Shaked, Phys. Rev. B **31**, 508 (1985).
[4] G. André, P. Bonville, F. Bourée, A. Bombik, M. Kolenda, A. Oleś, A. Pacyna, W. Sikora, and A. Szytula, J. Alloys Compd. **224**, 253 (1995); **232**, 307 (1996).
[5] S. L. Bud'ko and P. C. Canfield (unpublished).
[6] W. Rieger and E. Parthé, Monatsch. Chem. **100**, 444 (1969).
[7] F. Bourée-Vigneron, Phys. Scr. **44**, 27 (1993).
[8] According to the paper (Ref. 7) the modulation vector is $(0\ \ 0\ \ \frac{1}{4})$ with respect to the Brillouin-zone (BZ) boundary. Here we mention that our definition of a propagation vector is made with respect to the center (Γ) of BZ which has the full point-group symmetry of the space group of the underlying crystal structure.
[9] A. J. Freeman, *Magnetic Properties of Rare Earth Metals*, edited by R. J. Elliot (Plenum, New York, 1972), Chap. 6, p. 245.
[10] G. Czjzek, V. Oestreich, H. Schmidt, K. Lątka, and K. Tomala, J. Magn. Magn. Mater. **79**, 42 (1989).
[11] P. C. Canfield and Z. Fisk, Philos. Mag. B **56**, 1117 (1992).
[12] T. Shigeoka, H. Fujii, M. Nishi, Y. Uwatoko, T. Takabatake, I. Oguro, K. Motoya, N. Iwata, and Y. Ito, J. Phys. Soc. Jpn. **61**, 4559 (1992).
[13] J. A. Blanco, D. Gignoux, D. Schmitt, and C. Vettier, J. Magn. Magn. Mater. **97**, 4 (1991).
[14] Per Bak and J. von Boehm, Phys. Rev. B **21**, 5297 (1985).
[15] J. P. Hannon, G. T. Trammel, M. Blume, and D. Gibbs, Phys. Rev. Lett. **61**, 1245 (1988).
[16] J. P. Hill and D. F. McMorrow, Acta Crystallogr., Sect. A: Found. Crystallogr. **A52**, 236 (1996).
[17] C. Detlefs, A. I. Goldman, C. Stassis, P. C. Canfield, B. K. Cho, J. P. Hill, and D. Gibbs, Phys. Rev. B **53**, 6355 (1996).
[18] C. Detlefs, A. H. M. Z. Islam, A. I. Goldman, C. Stassis, P. C. Canfield, J. P. Hill, and D. Gibbs, Phys. Rev. B **55**, R680 (1997).
[19] P. M. Gehring, L. Rebelsky, D. Gibbs, and G. Shirane, Phys. Rev. B **45**, 243 (1992).

[20] D. Gibbs, D. R. Harshman, E. D. Isaacs, D. B. McWhan, D. Mills, and C. Vettier, Phys. Rev. Lett. **61**, 1241 (1988); D. Gibbs, G. Grübel, D. R. Harshman, E. D. Isaacs, D. B. McWhan, D. Mills, and C. Vettier, Phys. Rev. B **43**, 5663 (1991).

[21] The agreement index *R*-Bragg is calculated according to $R\text{-Bragg} = (\Sigma|I_{Obs}-I_{Cal}|)/\Sigma I_{Obs}$.

[22] The transformation matrix for the Miller indices referred to the conventional unit-cell axes ($\hat{\mathbf{a}}$, $\hat{\mathbf{b}}$, $\hat{\mathbf{c}}$) to those [see Table II, column $(h\ k\ l)_m$] referred to the magnetic unit-cell axes ($2\hat{\mathbf{a}}$, $2\hat{\mathbf{b}}$, $4\hat{\mathbf{c}}$) is given below:

$$\begin{pmatrix} 2 & 0 & 0 \\ 0 & 2 & 0 \\ 0 & 0 & 4 \end{pmatrix}.$$

[23] One way to probe such a small induced moment, if it exists, is by making XRES sensitive to Ni moments. In this case one needs to look for the quadrupole resonance below the Ni *K* edge (see Refs. 43,44).

[24] A. Szytula, A. Oleś, Y. Allain, and G. André, J. Magn. Magn. Mater. **75**, 298 (1988).

[25] Z. Islam, C. Detlefs, C. Song, A. I. Goldman, S. L. Bud'ko, P. C. Canfield, K. Finkelstein, J. P. Hill, and D. Gibbs, XRES measurements (unpublished).

[26] Z. Islam, C. Detlefs, A. I. Goldman, S. L. Bud'ko, P. C. Canfield, and A. Zheludev, Solid State Commun. (to be published); see also Ref. 4.

[27] J. K. Yakinthos, J. Magn. Magn. Mater. **99**, 123 (1991).

[28] R. J. Elliot, Phys. Rev. **124**, 346 (1961).

[29] T. A. Kaplan has also independently developed a mean-field theory using a simplified Hamiltonian and arrived at similar conclusions; see Phys. Rev. **124**, 329 (1963).

[30] This is to be expected on general grounds according to Nernst's theorem.

[31] R. J. Elliot, *Magnetism*, edited by G. T. Rado and H. Suhl (Academic, New York, 1965), Vol. IIA, Chap. 7, p. 401.

[32] J. A. Blanco, D. Gignoux, and D. Schmitt, Z. Phys. B **89**, 343 (1992).

[33] M. Hogh Jensen and Per Bak, Phys. Rev. B **27**, 6853 (1983).

[34] Walter Selke and Michael E. Fisher, Phys. Rev. B **20**, 257 (1979).

[35] The $D_{J=6}$ manifold of Tb^{3+} decomposes into even irreducible representations of the D_{4h} point group as follows: $D_6 = 2\Gamma_1^+ \oplus \Gamma_2^+ \oplus 2\Gamma_3^+ \oplus 2\Gamma_4^+ \oplus 3\Gamma_5^+$, where Γ_5^+ is a doublet and the rest are singlet representations. See G. F. Koster, J. O. Dimmock, R. G. Wheeler, and H. Statz, *Properties of the Thirty-Two Point Groups* (M.I.T. Press, Cambridge, Massachusetts, 1963), Tables 37 and 41.

[36] B. Bleaney, Proc. R. Soc. London, Ser. A **276**, 19 (1963).

[37] G. T. Trammel, Phys. Rev. **131**, 932 (1963).

[38] G. E. Bacon, *Neutron Diffraction* (Oxford, London, 1962).

[39] W. Marshall and S. W. Lovesey, *Theory of Thermal Neutron Scattering* (Oxford, London, 1971).

[40] Linear absorption coefficient (μ) calculated from macroscopic coefficients given in Ref. 42 scaled according to $1/v$ law and weighted appropriately for $TbNi_2Ge_2$ is 0.493 (cm^{-1}). For a cylindrical sample radius of 0.9 cm μR is 0.44; Absorption factors for various angles were then interpolated from the table given by Bradley (Ref. 45).

[41] Gen Shirane, Acta Crystallogr. **12**, 282 (1959).

[42] *International Tables for Crystallography*, edited by A. J. C. Wilson (Kluwer Academic, Dordrecht, 1995), Vol. C, Chap. 4, Sec. 4.

[43] K. Namikawa, M. Ando, T. Nakajima, and H. Kawata, J. Phys. Soc. Jpn. **54**, 4099 (1985).

[44] J. P. Hill, C.-C. Kao, and D. F. McMorrow, Phys. Rev. B **55**, R8662 (1997).

[45] A. J. Bradley, Proc. Phys. Soc. London **47**, 879 (1935).